Long-term monitoring of wind field characteristics and dynamic response of a long-span suspension bridge in complex terrain

Aksel Fenerci, Ole Øiseth, Anders Rönnquist

Department of Structural Engineering, Norwegian University of Science and Technology, Trondheim, Norway

Keywords: suspension bridge; bridge monitoring; field measurement; wind characteristics; response surface methodology; complex terrain; bridge dynamic response

Abstract

Long-term monitoring data of wind velocities and accelerations on the Hardanger Bridge are used to investigate the relationship between the wind-loading and response processes. The extensive measurement system consisting of 20 accelerometers and 9 anemometers is described as well as the local topography of the site. The wind and response characteristics are presented using scatter plots and wind rose diagrams. The considerable variability observed in the bridge dynamic response is investigated by utilizing response surface methodology. Simple parameters of the wind field are selected as the predictor variables in the analyses. The variability in response is attributed to the variable wind field, and the effects of the significant parameters on the response are presented in a statistical framework. The agreement of the findings with previous considerations and the implications on the design of long-span suspension bridges are discussed.

1. Introduction

The Norwegian Public Roads Administration (NPRA) is currently seeking solutions to replace several ferry connections along Norway's coastal highway E39 with road transportation. The extraordinary terrain typical of the west coast of Norway, famous for its fjords and tall mountains, requires crossing straits up to 5 km long and 2 km deep, which manifests a challenging task for bridge engineers. The growing demand for longer suspension bridges around the world calls for relatively lighter and slenderer bridge structures, which will be prone to excessive wind excitation. To this day, many bridges exhibited

unexpected behavior due to different wind-related phenomena, such as flutter [1], vortex shedding [2] and excessive cable vibrations [1,3], which revealed gaps in the knowledge of loading mechanisms on such structures. To diagnose and minimize these unexpected effects, monitoring of existing structures and analysis of field data are deemed essential [4].

Accurate prediction of wind-induced response of suspension bridges is vitally important for reliable design and assessment of such structures. Predicting the dynamic response, however, accommodates uncertainties due to many sources, including the modeling of gust loading. Following the work of Davenport [5], the dynamic load effects caused by atmospheric turbulence are traditionally described using power spectral densities (PSDs) and coherences of turbulence [6–9]. Consequently, several expressions have been suggested for the spectral densities over the years [6,10,11], which in general depend on basic parameters of the wind field. The results of the recent bridge monitoring efforts [12–16] reveal that the wind field characteristics exhibit variability from site to site. Therefore, the spectral expressions need to be adjusted for the site in question using field measurements [13,17]. The site-specific spectra are generally deduced from single events such as typhoons or averaged over a number of recordings. However, neither approach seems to reflect the actual variability of the wind field present at the particular site, making it difficult to establish design spectra, even for a specific site. Solari and Piccardo [18] presented a collection of wind field statistics taken from field measurement results in the literature. The variability of the results presented by [18], as well as the random and site-dependent nature of wind loading on suspension bridges, encourage a probabilistic description of the wind field [19–21].

The field measurement results of wind statistics and structural responses were reported by several researchers as the outcomes of large measurement campaigns to investigate the effect of wind loading on bridge response and modal properties [4,14,22–24] or to verify numerical simulations [17,25–27]. The studies showed that reasonable predictions of dynamic response can be achieved using the measured turbulence spectra. Other works showed that the spectra can accommodate significant uncertainty and that the selection can significantly influence the response estimations [9,28].

In complex terrain, the wind field is expected to be variable and not homogenous. However, modeling the wind field using state-of-the-art methods will not reflect this variability in the dynamic response

predictions. Consequently, safety concerns may arise when designing very long suspension bridges. The present study aims to put forth the actual relationship between wind and the response parameters of a long-span suspension bridge located in complex terrain using long-term field data. The thorough analysis of wind field parameters and their effects on the dynamic response will provide insight into the uncertainties involved in wind field modelling and response prediction. For this purpose, field measurement results are presented from an extensive monitoring system installed on the Hardanger Bridge in Norway. The wind and response characteristics for the measurement period are presented. The influence of the wind field on the dynamic response is studied in a statistical framework, using response surface methodology (RSM) with basic wind-related parameters from measurements. The significance of the parameters is assessed using hypothesis testing techniques. Finally, the effects of the significant wind field parameters are presented in the form of two-dimensional surface plots.

2. The Hardanger Bridge and its surroundings

The Hardanger Bridge (Fig. 1) crosses the Hardangerfjord in Hordaland county of Norway, connecting the small towns of Bu and Vallavik (Fig. 2). Since its completion in 2013, it remains the longest suspension bridge in Norway with its slender main span of 1310 meters. The bridge deck has a well-streamlined box shape and guide vanes were installed underneath the deck to mitigate vortex-induced vibrations. The bridge girder is 18.5 meters wide and 3.2 meters high, supporting two traffic lanes and a bicycle lane, making the bridge exceptionally slender compared to existing structures with similar scales. The bridge direction deviates approximately 25˚ from the north-south direction, towards the west, perpendicular to the fjord. The bridge is surrounded by steep mountains (1000-1500 meters high) to the north and the south. The view of the surrounding fjords and mountains is shown Fig. 3.

The dynamic characteristics of the Hardanger Bridge, namely its natural frequencies and mode shapes are extracted from a finite element (FE) model of the bridge through eigenvalue analysis. The FE model was provided by NPRA. According to the analysis, the first lateral symmetric mode occurs at 0.05 Hz, followed by an antisymmetric lateral mode at 0.098 Hz. The first vertical asymmetric and symmetric frequencies of the structure were calculated as 0.11 Hz and 0.14 Hz, respectively. The first torsional

vibration frequency was 0.36 Hz. The fundamental frequencies of the structure under 16 m/s wind were also identified by [29], using Operational Modal Analysis (OMA). The results were similar to the FE analysis.

Fig. 1. The Hardanger Bridge

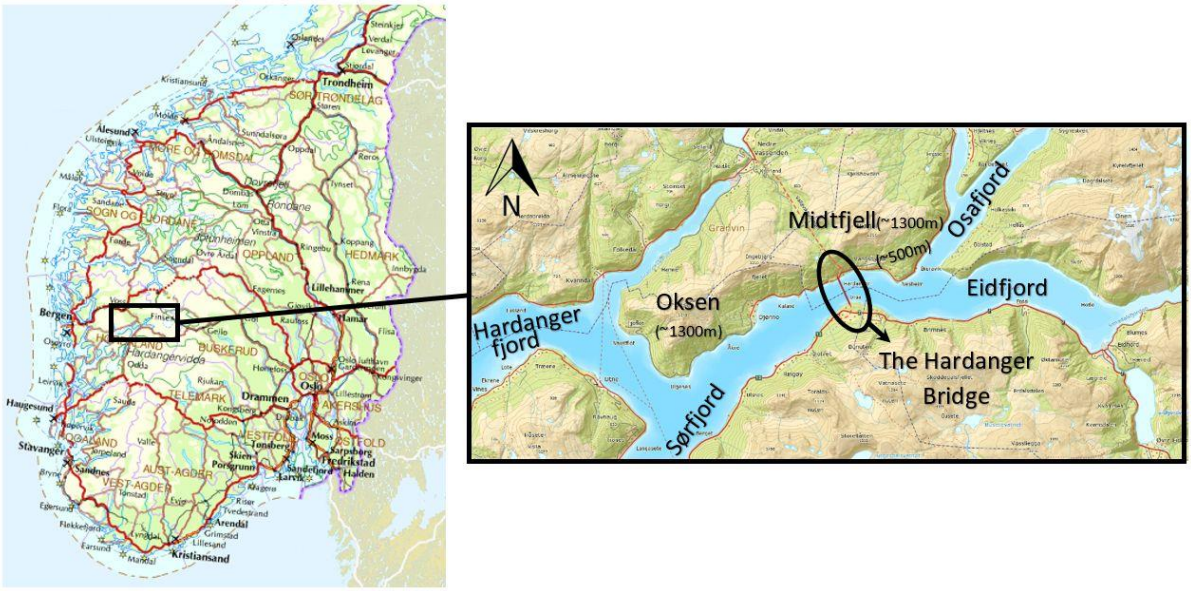

Fig. 2. Location and local topography (map images from Kartverket©)

(a)

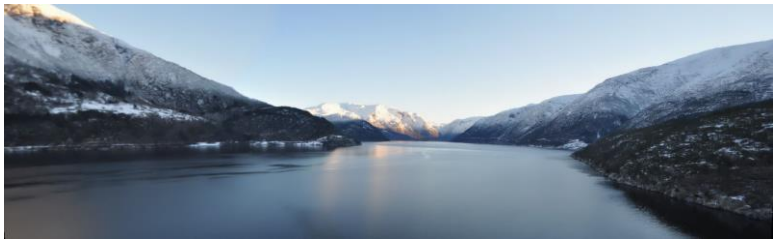

(b)

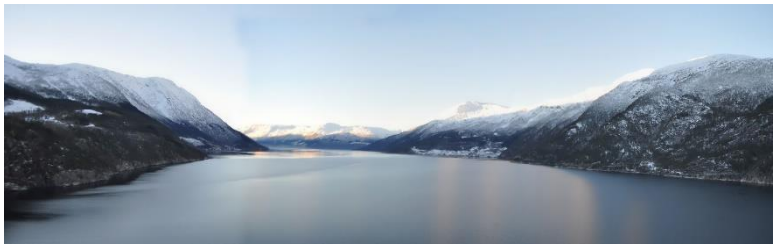

Fig. 3. View from the Hardanger Bridge (a) towards the east and (b) towards the west

3. The Measurement System

The Hardanger Bridge was instrumented with an extensive monitoring system after its completion to measure the wind velocities and dynamic excitation at several locations on the bridge girder and the bridge towers. The monitoring system is shown in Fig. 4 on a scale drawing of the Hardanger Bridge. The sensor network consists of 9 sonic anemometers and 20 triaxial accelerometers. WindMaster Pro 3D anemometers were used to measure the wind speeds; these are robust triaxial ultrasonic anemometers capable of measuring wind gusts up to 65 m/s. CUSP-3D series strong motion accelerometers with a ± 4g measurement range were used for the acceleration measurements. The names and coordinates of all the sensors are listed in Table 1; the midspan of the bridge was selected as the origin of the coordinate system. 16 of the accelerometers are located inside the bridge girder, attached on bulkheads on both sides of the girder to capture the torsional motion, while the remaining 4 are located inside the bridge towers. Anemometers A1-8 are attached to bridge hangers at a height of 8 meters above the girder, except for one anemometer (A6) that is attached to a light pole at the midspan. As shown by the sensor layout presented in Fig. 4, the accelerometers were distributed uniformly along the bridge girder, whereas the anemometers were unevenly distributed. This layout was intentionally selected to extract more information about the spatial structure of the wind field at the site. The final anemometer (A9) is located at the top of the Vallavik (North) Tower.

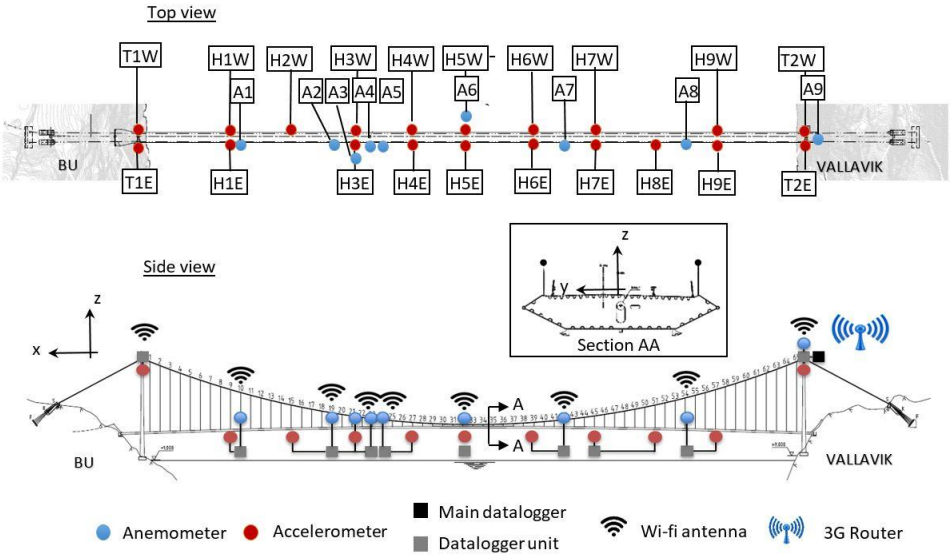

Fig. 4. The measurement system

Each sensor is connected to a datalogger unit, where the data are recorded locally, then the data are transferred to a main datalogger located at the top of the Vallavik Tower (Fig. 4) by wireless communication. A CUSP-Me series recorder was used for the main datalogger, while the other dataloggers were of type CUSP-Ms. Both types are suitable for working with a variety of different sensors. The time synchronization of the data was ensured by using GPS time. The data collected at the main logger unit are then transferred to servers at the Norwegian University of Science and Technology (NTNU) via an internet connection and are stored there. Pictures of sensors are shown in Fig. 5.

(a) 

(b) 

Fig. 5. Instruments on the bridge: (a) triaxial accelerometer inside the bridge deck and (b) anemometer attached to the hanger

The wind velocities and accelerations at the Hardanger Bridge site were recorded starting from December 2013, and the monitoring campaign is still ongoing. This study considers recordings from December 2013 to March 2016, corresponding to a total of 28 months. During this period, the sensors were operational; however, the data were only stored after a triggering wind speed of 15 m/s was exceeded in any of the wind sensors. After the system was triggered, the accelerations and wind

velocities were recorded for a duration of 30 minutes. The system was also triggered manually several times in a random manner during this period, to include recordings with lower wind speeds in the dataset. The dataset which will be used throughout the rest of the paper consists of 9590 10-minute long recordings. A histogram showing the distribution of recordings according to the mean wind velocity is given in Fig. 6.

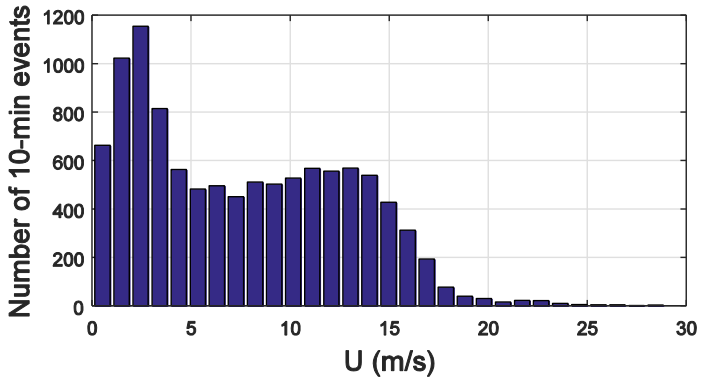

Fig. 6. Histogram of 10-minute recordings

Table 1
Sensor names and coordinates

Wind sensors				Accelerometers			
Name	x (m)	y (m)	z (m)	Name	x (m)	y (m)	z (m)
A1	460	7.25	0.3	H1E/H1W	480	6.33/-6.64	-8.38
A2	280	7.25	3.2	H2W	360	-6.64	-6.41
A3	240	7.25	3.9	H3E/H3W	240	6.33/-6.64	-4.45
A4	200	7.25	4.6	H4E/H4W	120	6.33/-6.64	-2.48
A5	180	7.25	4.9	H5E/H5W	-7	6.33/-6.64	-0.4
A6	-10	-7.25	8	H6E/H6W	-120	6.33/-6.64	-2.25
A7	-180	7.25	5.2	H7E/H7W	-240	6.33/-6.64	-4.22
A8	-420	7.25	1.2	H8E	-360	6.33	-6.18
A9	-655	4.5	140	H9E/H9W	-480	6.33/-6.64	-8.15
				T1E/T1W	655	4.5/-4.5	120.5
				T2E/T2W	-655	4.5/-4.5	120.5

4. Wind Characteristics

4.1 Data handling

The wind velocities at the Hardanger Bridge site were recorded in polar coordinates with a sampling frequency of 32 Hz using the nine anemometers mentioned above. The wind data were then resampled to 20 Hz and decomposed into static (mean wind velocity, U) and dynamic (wind velocity fluctuations) components considering a 10-minute averaging interval, where the wind process was assumed to be stationary [6,8]. The three wind velocity fluctuations are referred as the along-wind (u), cross-wind (v) and vertical (w) turbulence components. All the one-point statistics used to characterize the wind field are calculated using the wind measurements at the midspan (sensor A6).

Sample time series of the turbulence components and wind direction are given in Fig. 7 for a 10-minute interval, which was recorded on January 12, 2015, starting at 17.43 local time. The turbulence spectra of the along-wind and the vertical components are estimated using the same 10-minute recording. Welch spectral estimation method is used with 8 data segments with 50% overlap. A Hamming window is applied to each segment prior to averaging. The respective von Karman spectra [11] are also calculated and both spectra are given in Fig. 8 to present the diversity of the spectral shapes. It is observed that the von Karman spectra represents the along-wind turbulence reasonably well, where some discrepancies are present for the vertical turbulence. The measured vertical turbulence is rather flat in the 0.1-1 Hz frequency range, which is observed commonly in the rest of the database; however, the slope of the two spectra agrees for higher frequencies. To avoid any disturbance of the wind flow due to the presence of the bridge deck and the vehicles on travelling on it, the anemometers were installed 8 meters above the deck. It is also important to ensure that the wind speed measurements are not affected by the structural vibrations of the bridge deck. Any such effect would be detectable as peaks on the wind spectra at the locations of the natural frequencies of the bridge. Looking at the measured wind spectra (Fig. 8), no such peaks were observed, even for high response levels. Furthermore, the maximum instantaneous velocity of the girder was calculated approximately as 0.5 m/s by integrating the accelerometer signals for the highest measured response.

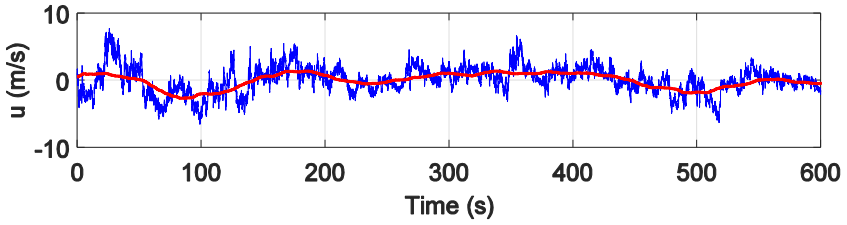

(a)

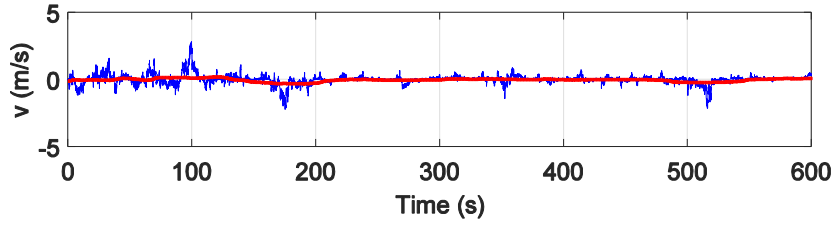

(b)

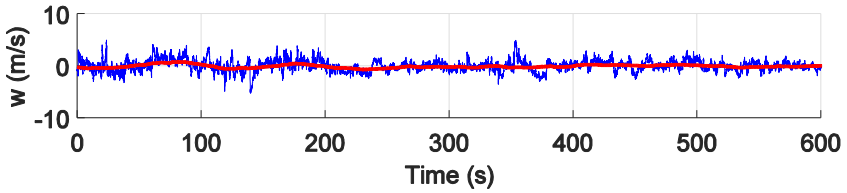

(c)

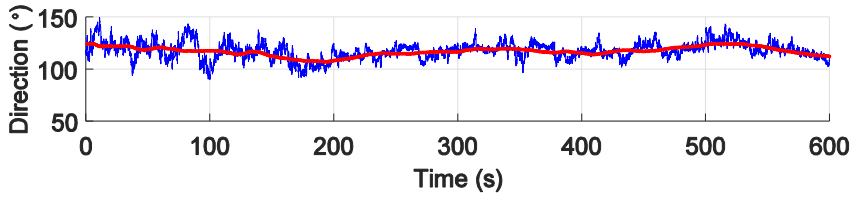

(d)

Fig. 7. Sample time series of wind measurements (U = 15.6 m/s) recorded on 12/1/2015: (a) along-wind turbulence (b) cross-wind turbulence (c) vertical turbulence and (d) wind direction

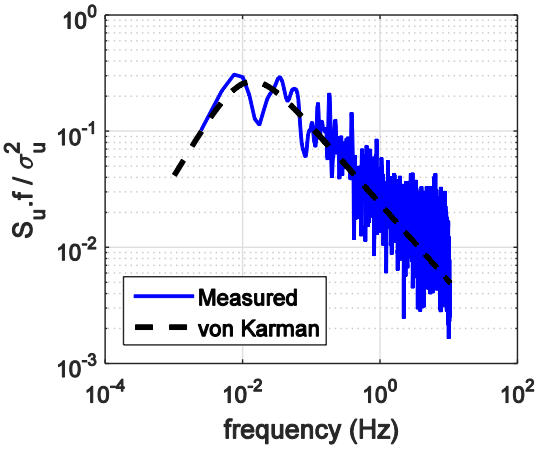

(a)

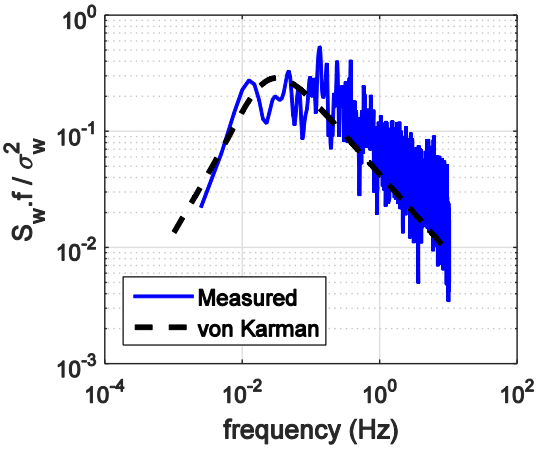

(b)

Fig. 8. Spectral density estimates of turbulence components for a 10-minute recording on 12/1/2015: (a) along-wind turbulence and (b) vertical turbulence

A running mean is also plotted on the time series to highlight any non-stationary behavior. It is observed that the along-wind turbulence component exhibits non-stationary behavior, which is frequently observed also in the rest of the data. Although non-stationary models can also be used to study the wind characteristics [30–32], the traditional stationary wind model is preferred here due to its common use in practice. Recent case studies based on typhoon winds [30,32] also show that if there is no sudden change in the wind direction or no rapid increase or decrease is present in the wind speed (such as in the build-up phase of a storm), the difference between stationary and non-stationary wind characteristics is not significant. For the strong winds recorded at the Hardanger Bridge, 10 minutes duration is sufficient to exclude such variations in the wind speed and the wind direction is usually steady.

4.2 Mean wind speed and direction

The mean wind velocities (U) were calculated for 10-minute intervals for all recordings using the sensor at the midspan (A6) and are presented in the wind rose plot shown in Fig. 9, using a threshold wind speed of 3 m/s. The wind rose was plotted on top of the topographical map of the bridge site to show the influence of local topography on the wind conditions. The 0˚ direction shown in Fig. 9 is the bridge direction. The results suggest that the wind was approaching from either the east or the west and was mainly perpendicular to the bridge girder. The easterly winds approached the bridge from a wider

directional range compared to the westerly winds. The directions of the easterly winds were bounded by the surrounding mountains; the highest mean speeds from this direction were approximately 18 m/s, and no significant directional dependence was observed. The westerly winds, on the other hand, had higher mean speeds of up to 30 m/s with mean directions almost perpendicular to the bridge direction.

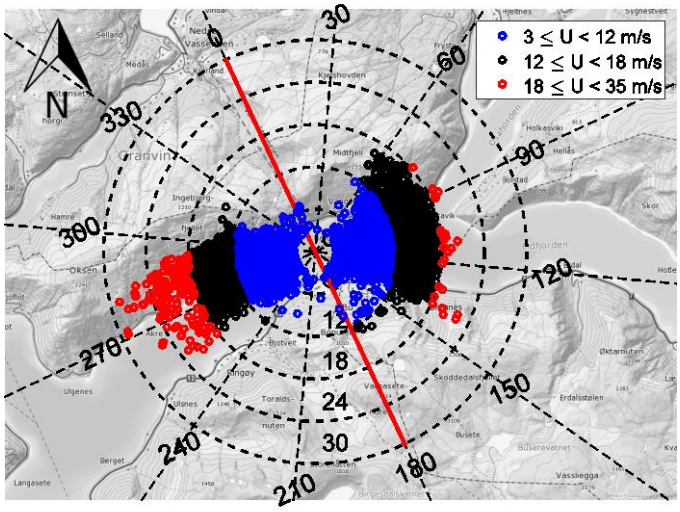

Fig. 9. Wind Rose plot of 10-min mean wind velocity (m/s)

4.3 Turbulence intensity

The turbulence intensity is a simple indicator of the intensity of the atmospheric turbulence. For the three turbulence components (u, v, w), the turbulence intensity is defined as

$$I_u = \frac{\sigma_u}{U}, I_v = \frac{\sigma_v}{U}, I_w = \frac{\sigma_w}{U} \quad (1)$$

where σ_u, σ_v and σ_w denote the standard deviations of the turbulence components. The turbulence intensity factors for each of the three turbulence components were calculated for the 10-minute intervals, and wind rose plots were generated as shown in Fig. 10. The plots reveal that for the lower speed winds, the results are rather arbitrary, and the turbulence intensities are scattered randomly. This is due to the fact that the lower wind speeds accommodate more non-stationary behavior due to sudden changes in the wind direction and mean wind speed. In addition, since the wind speed fluctuations are divided by the mean wind speed in calculation of the turbulence intensity, similar variations in wind fluctuations result into larger scatter in case of low wind speeds. However, when strong winds are considered, the scatter is much smaller, and more dependence on the wind direction is observed. The

along-wind turbulence intensity (I_u) ranges between 10% and 35% for strong winds (U > 12 m/s) from either direction. The cross-wind (I_v) and vertical (I_w) turbulence intensities exhibited much smaller values, ranging between 0-15 % for the strong winds. The vertical turbulence intensity is more dependent on the wind direction than the along-wind turbulence (Fig. 10c). For the easterly winds, the 60˚- 90˚ range, where the wind flow had passed over a hill, generated the most turbulent flows. For the westerly winds, the winds blowing along the fjord, which were believed to be disturbed previously by the foothills of Mountain Oksen, had more vertical turbulence intensity (Fig. 2).

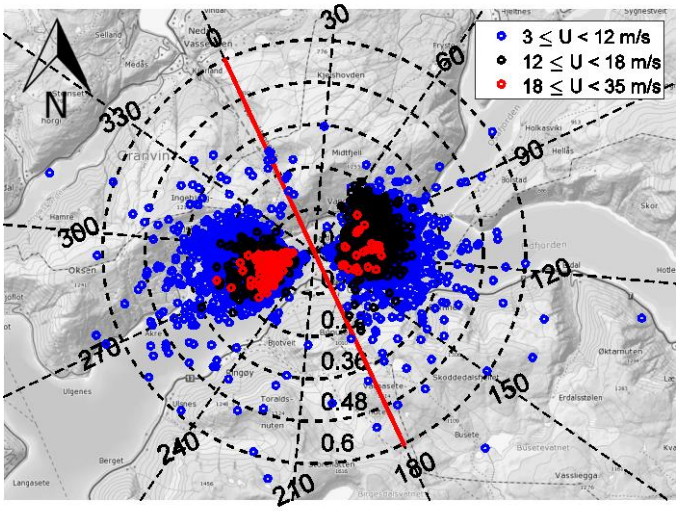

(a)

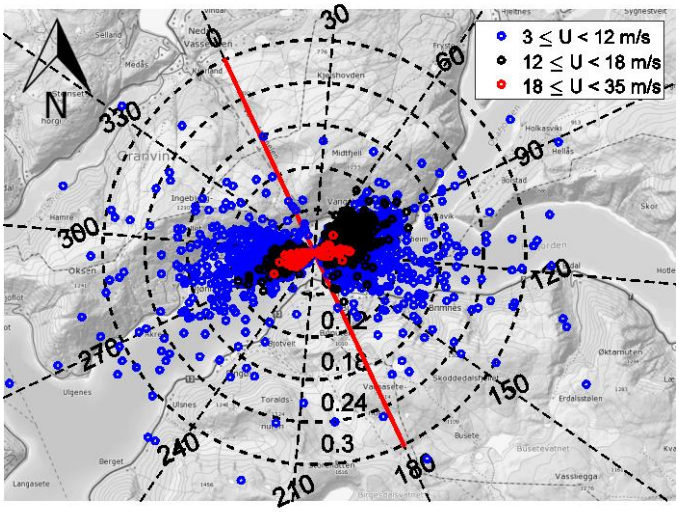

(b)

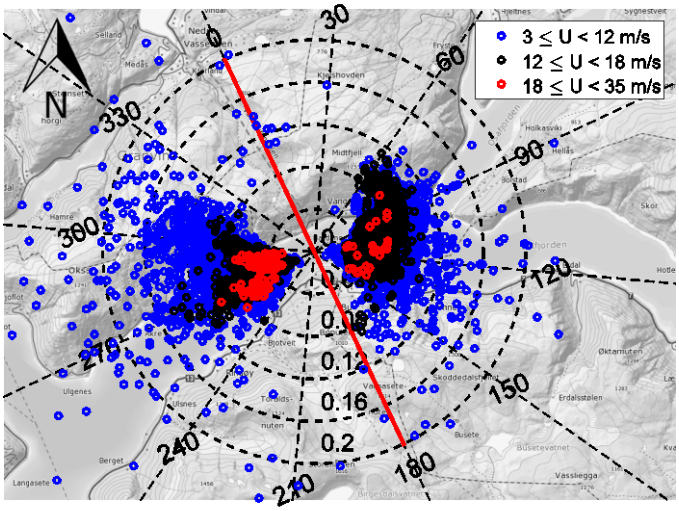

(c)

Fig. 10. Wind rose plots of turbulence intensities: (a) along-wind turbulence intensity, (b) cross-wind turbulence intensity and (c) vertical turbulence intensity.

The covariance of the u and w turbulence components were plotted similar to the turbulence intensities (Fig. 11). Covariance of the turbulence components were calculated using

$$\mathrm{cov}(u,w) = \frac{1}{N-1}\sum_{i=1}^{N}(u_i - \mu_u)^*(w_i - \mu_w) \tag{2}$$

where N denotes the number of observations, $\mu_{u,w}$ denote the mean of turbulence components and * denotes the complex conjugate operation. The wind rose diagrams were separated into positive and negative correlations; most of the data indicated positive correlation of the two components, contradicting previous theoretical considerations [10,33]. However, similar observations have been reported previously [34,35]. For the westerly winds, the covariance term was positive for the winds blowing along the fjord (240-270˚) and negative for the winds from the mountain direction (270-300˚), demonstrating good separation. Smaller values were generally obtained from the easterly winds, for which no directional dependence was observed.

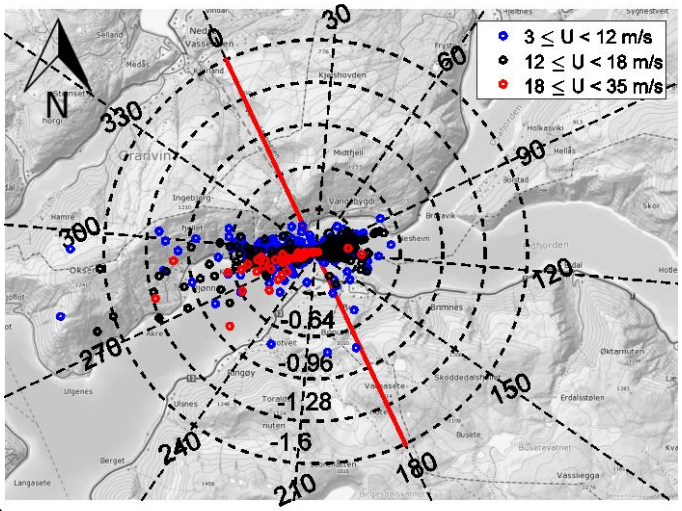

237 (a)

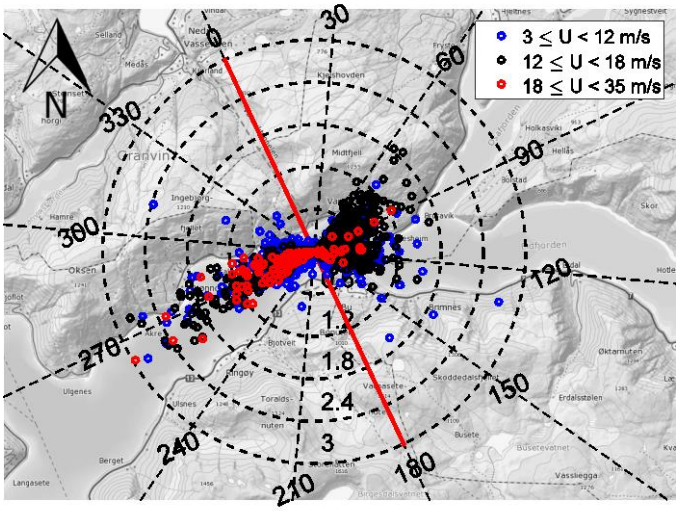

238 (b)

239 Fig. 11. Wind rose plots of the covariance term of longitudinal (u) and vertical (w) turbulence
240 components (a) negative correlation (b) positive correlation

241 ## 4.4 Turbulence length scale

242 The turbulence length scale or the integral length scale ($L_{u,v,w}$) represents the spectral content of the
243 turbulence and can therefore be interpreted as the average eddy size of the turbulence. Theoretically,
244 nine different length scales, three for each of the turbulence components, can be defined for the three-
245 dimensional atmospheric turbulence. The length scale for the u-component in the along-wind direction
246 can be written as [6]

247 $$L_u = \frac{1}{\sigma_u^2}\int_0^\infty R_{uu}(x)dx \qquad (3)$$

where $R_{uu}(x)$ is the spatial cross-covariance function of the u-component. The same definition applies to the other turbulence components. Due to their physical interpretation, the length scales are essential parameters for describing atmospheric turbulence. In practice, the length scales cannot be calculated using Eqn. (3), so they have to be estimated using approximate techniques [6]. However, estimating length scales from field data appears to be troublesome; the length scale estimates reported by previous studies show enormous variability in magnitude. After studying many field estimates of length scales in near-neutral atmospheric conditions, Solari [18] reported that the variability was not solely due to the terrain of interest, but also due to the estimation approach adopted. To examine the variability of estimates for the site in question, two practical estimation methods were adopted in this study. The first method (method 1) calculates the length scale by aligning the peak of the measured turbulence spectrum with the von Karman spectrum [11], which was given as

$$\frac{f\,S_u(f)}{\sigma_u^{\,2}} = \frac{4\dfrac{L_u f}{U}}{\left[1+70.8\left(\dfrac{L_u f}{U}\right)^2\right]^{5/6}}, \qquad \frac{f.S_w(f)}{\sigma_w^{\,2}} = \frac{4\dfrac{L_w f}{U}\left[1+755\left(\dfrac{L_w f}{U}\right)^2\right]}{\left[1+283\left(\dfrac{L_w f}{U}\right)^2\right]^{11/6}} \tag{4}$$

for the along-wind and vertical turbulence components. The second method (method 2) integrates the auto-covariance function of the turbulence component up to the first zero crossing, assuming that Taylor's hypothesis is valid [6]. The relation for the longitudinal length scale then becomes

$$L_u = \frac{U}{\sigma_u^{\,2}}\int_0^{\infty} R_{uu}(\tau)d\tau, \quad R_{uu}(\tau) = \lim_{T\to\infty}\frac{1}{T}\int_{-T/2}^{T/2} u(t)u(t+\tau)d\tau \tag{5}$$

where $R_{uu}(\tau)$ is the cross-covariance function of the turbulence component in time. Fig. 12 shows the wind rose plots of the longitudinal length scales for 10-minute intervals obtained using both methods, and the vertical length scale estimates are given in Fig. 13. Although estimating the length scales is fundamentally important for describing the atmospheric turbulence, the results indicate significant discrepancy in terms of magnitudes. The estimates of method 2 are systematically larger than those of method 1. The patterns in Fig. 12a and Fig. 12b, on the other hand, are in reasonable agreement with only minor differences. The general trends in Fig. 13a and Fig. 13b are also reasonably similar. The estimations of method 1 were clearly larger for the winds travelling along the fjord, where the winds

were bounded by the mountains, while method 2 gave relatively more scattered results. Considering the values obtained using method 2, the longitudinal length scale of the strongest winds varies between 200 and 700 m, and the vertical length scale varies between 100 and 250 m. The length scale magnitudes obtained using method 2 show better agreement with the previously reported values [6]. In general, the longitudinal length scale was approximately 2-2.5 times the vertical length scale for both methods, which was in agreement with the observations of [8]. The wide range of the calculated length scale values, even for similar wind speeds and directions, implies that the spectral content of the turbulence varied randomly and therefore cannot be represented by a deterministic length scale value.

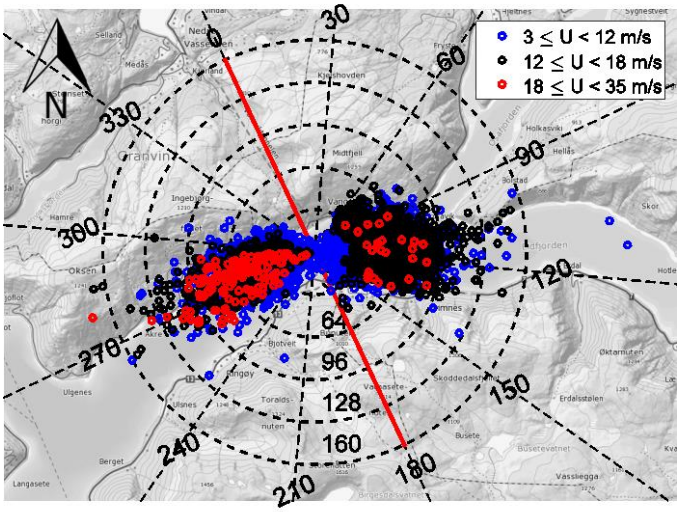

(a)

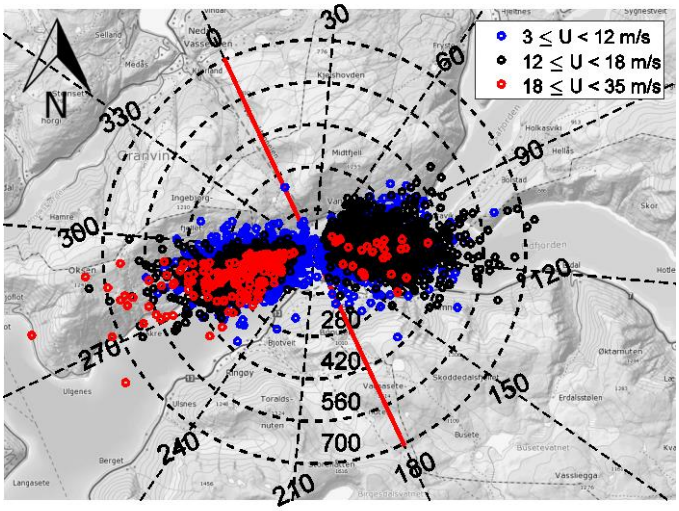

(b)

Fig. 12. Wind roses of the longitudinal length scale (L_u) estimates (in meters): (a) method 1 and (b) method 2

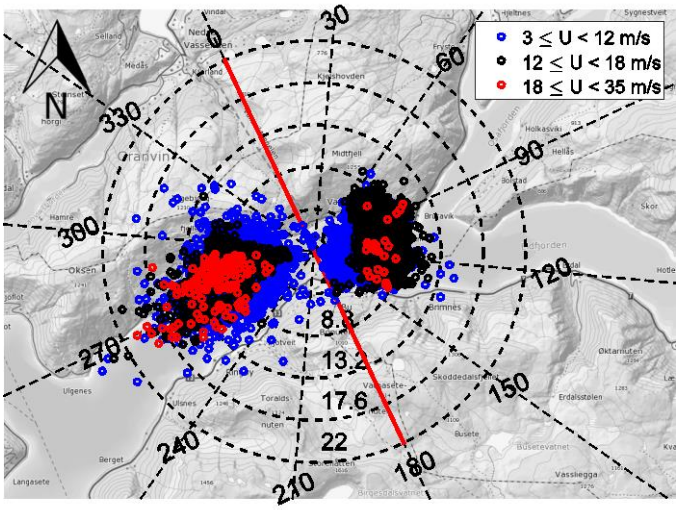

(a)

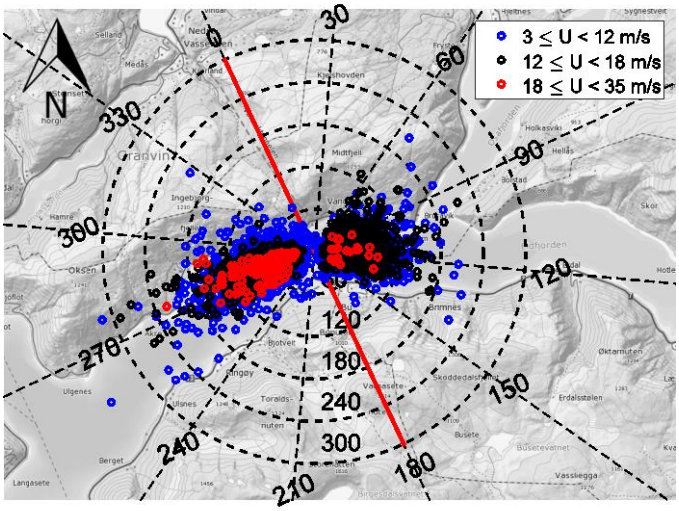

(b)

Fig. 13. Wind roses of the vertical length scale (L_w) estimates (in meters): (a) method 1 and (b) method 2

4.5 Angle of attack

The vertical angle of attack (β) is the angle between the mean wind velocity vector and the horizontal plane. Since the vertical inclination of the wind can influence the structural response, a brief description of the conditions at the site is useful. The angle of attack was calculated for each 10-minute interval, and a wind rose plot was generated to present the results. Negligible number of recordings exhibited negative angles with small amplitudes; therefore, only positive angles (mean wind velocity pointing upwards) are included in the figure. The results show that the mean wind velocity vector was generally inclined slightly upwards with angles of 1-5˚ for the strong winds.

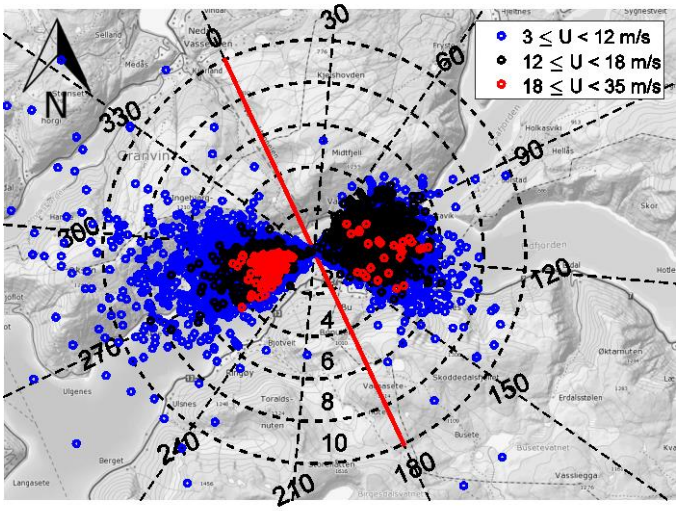

Fig. 14. Wind rose plot of the vertical angle-of-attack (β) in degrees

5. Response Characteristics

5.1 Data handling

The accelerations of the bridge girder were measured with a 200 Hz sampling frequency at 16 locations along the girder, as highlighted in Fig. 4. The acceleration data were then downsampled to 20 Hz, after applying a low-pass filter to avoid aliasing. The accelerometer pair located approximately at the midspan, namely H5E and H5W (Table 1), were selected to study the wind-induced dynamic response of the bridge girder. The vertical and lateral accelerations of the bridge girder were obtained by averaging the measurements from the two sensors, and the torsional response was obtained by dividing the difference of the two signals by the distance between the sensors. 10-minute long recordings, same as for the wind records, were used to calculate the RMS values of the acceleration components.

To effectively study the wind-induced response, other sources of vibration, such as traffic-induced vibrations, should be excluded from the analysis. Because the wind-induced response of a suspension bridge is typically in the 0-1 Hz frequency range [14,17,32], the vertical high frequency vibrations are expected to increase when there is traffic loading on the bridge [14]. Examining the acceleration data indicated that the dynamic response was dominated by low-frequency vibrations (below 1 Hz) when the wind speed was above 8 m/s. The recordings with low wind speed ($U < 8$ m/s) and high frequency content were removed from the dataset, assuming that the vibrations were induced by other sources

such as the overflowing traffic and are therefore outside of the scope of our analyses. Although the traffic density on Hardanger Bridge is typically low and the dynamic response is mainly due to wind (when wind speed is reasonably high), the effects of traffic loading could not be completely removed from the data. Therefore, other sources of vibration may still contribute to the overall variability in the results; however, this impact is expected to be negligible.

Spectral density estimations are given in Fig. 15 for the three response components for a 10-minute recording recorded on 12/1/2015, for which the wind time series were already given in Fig. 7. The spectra are estimated using Welch [36] spectral estimation method. Spectral estimates of 8 data segments with 50% overlap are computed using Fast Fourier Transform (FFT) and averaged after applying a Hamming window to each segment. It is seen that the responses are dominated by the fundamental modes, with some contribution from the higher modes. The lateral response spectra exhibits similar results for the rest of the database, with a typical large peak at the first symmetric lateral frequency (0.05 Hz) of the structure. On the other hand, significant contributions from several modes are commonly observed in case of the vertical and torsional responses.

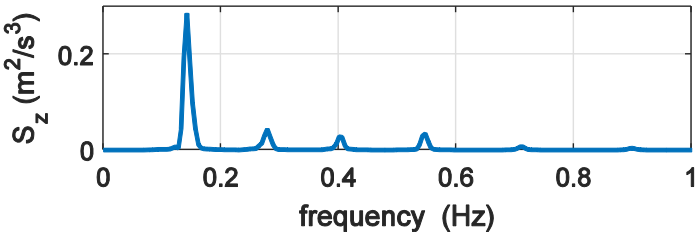

(a)

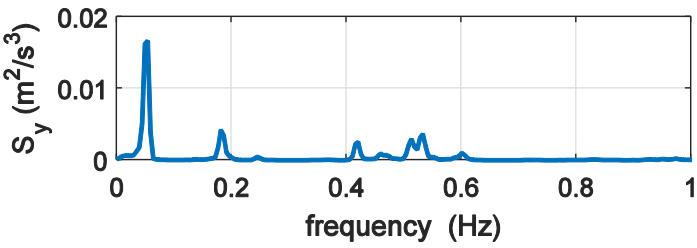

(b)

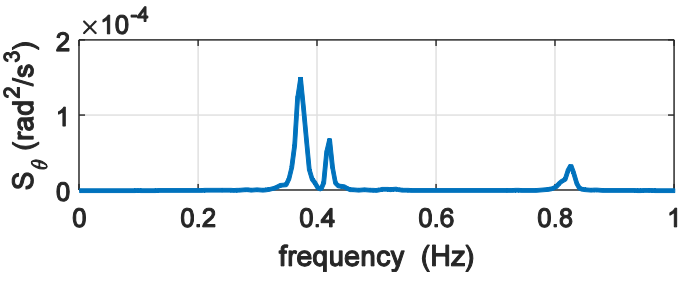

(c)

Fig. 15. Spectral density estimates of response components for a 10-minute recording on 12/1/2015: (a) vertical acceleration, (b) lateral acceleration and (c) torsional acceleration

5.2 Dynamic response due to wind

The measured root mean square (RMS) values for the lateral, vertical and torsional accelerations are presented in Fig. 16 in the form of wind rose diagrams. The easterly winds showed consistent patterns for the three response components. The dynamic response was usually higher for higher mean wind speeds and the perpendicular wind direction. Westerly winds, on the other hand, showed peculiar response characteristics. The lateral and vertical acceleration responses induced by the westerly winds were generally smaller than the vibrations measured for the easterly winds, where the torsional response was high but severely scattered. The largest measured torsional vibrations were caused by moderate winds (12 < U < 18 m/s) from the east. The most critical wind direction was apparently the range of 60˚-90˚, where the winds passed over a hill approximately 500-600 meters high (Fig. 2). The winds approaching from this range typically had high vertical turbulence (Fig. 10c) and small length scales (Fig. 12), likely due to the interaction with the terrain. This observation indicates the effect of the relatively high surface roughness along the 60˚-90˚ directional range on the response. However, the easterly winds travelling along the fjord with higher length scales did not cause large vibrations.

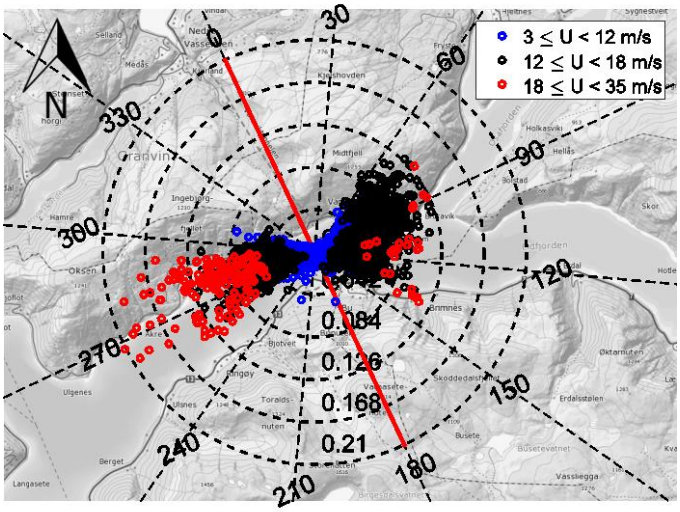

(a)

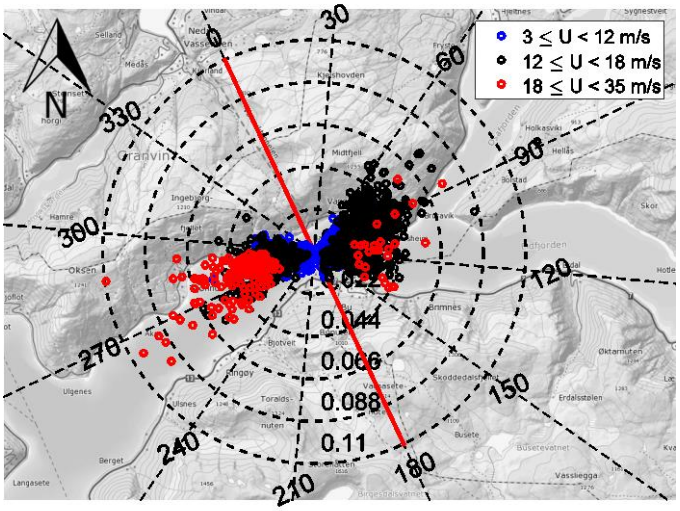

(b)

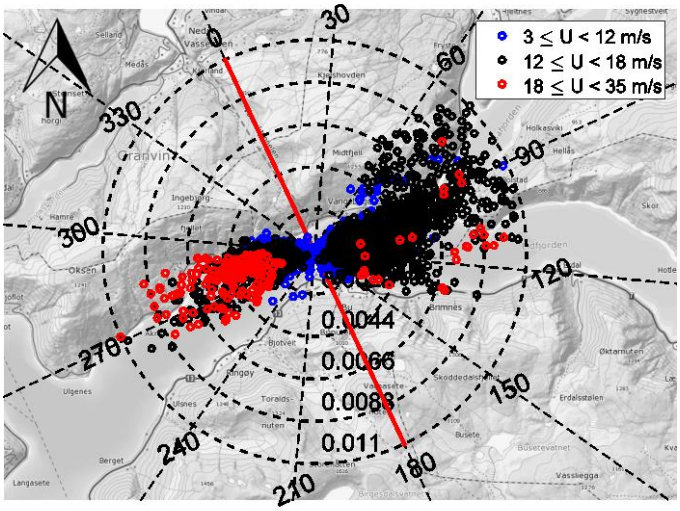

(c)

Fig. 16. Wind rose plots of the acceleration response: (a) RMS vertical acceleration (m/s^2) (b) RMS lateral acceleration (m/s^2) and (c) RMS torsional acceleration (rad/s^2)

The three response components were then plotted against mean wind velocity to demonstrate the general trend and the variability in the measurements (Fig. 17). The results indicate vast variability in the wind-induced dynamic response. The vertical response shows the least scatter and was greatly affected by the vertical turbulence intensity (Fig. 17a). More severe scatter is observed in the lateral response, which cannot be attributed to the variability in the along-wind turbulence alone (Fig. 17b). The torsional response shows the largest scatter of all (Fig. 17c), especially for winds with mean wind speeds exceeding 10 m/s In the moderate wind speed range (12-18 m/s), large torsional vibrations were observed. It is also seen that for high wind speeds, the torsional accelerations are separated. Higher

torsional accelerations were recorded when the vertical turbulence was high, which was mostly the case for the easterly winds, especially the wind approaching from the 60°-100° range, where the wind flow is disturbed by the mountains. The three response components are plotted in Fig. 18 again with color-coding for the easterly and westerly winds. Distinctive torsional behavior was observed for the two different wind directions, whereas the lateral and vertical responses were essentially similar for the easterly and westerly winds. The difference between the torsional responses for the easterly and westerly directions is mainly attributed to the terrain effects. High turbulence levels generated by the upwind terrain in the east resulted into larger torsional vibrations of the Hardanger Bridge deck.

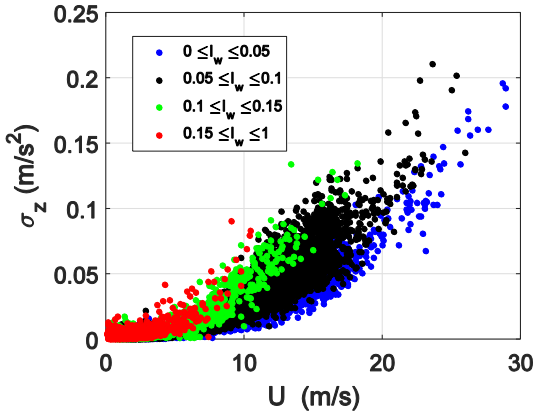

(a)

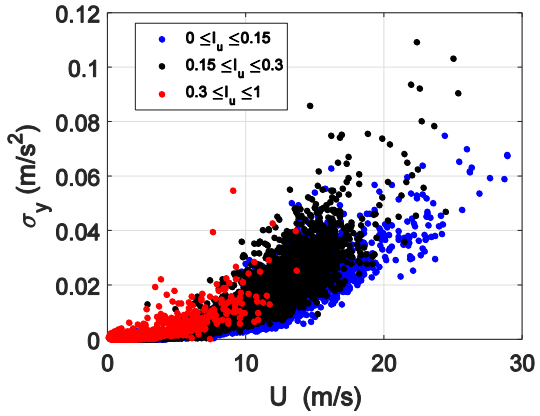

(b)

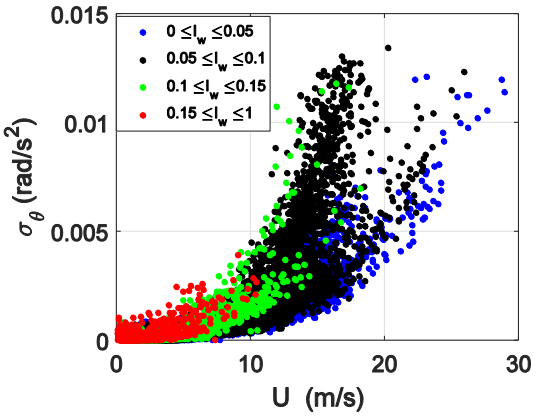

371 (c)

372

373 Fig. 17. RMS acceleration response plotted against mean wind velocity: (a) RMS vertical acceleration,

374 (b) RMS lateral acceleration and (c) RMS torsional acceleration

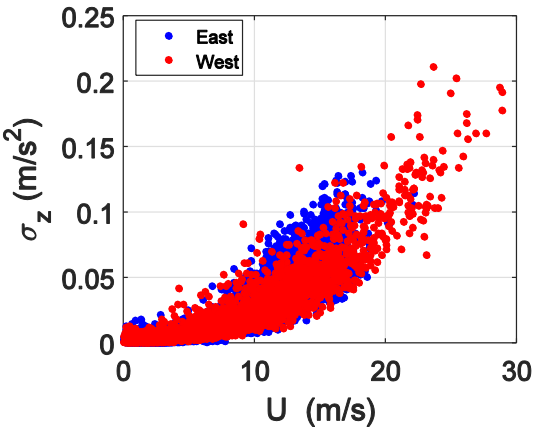

375 (a)

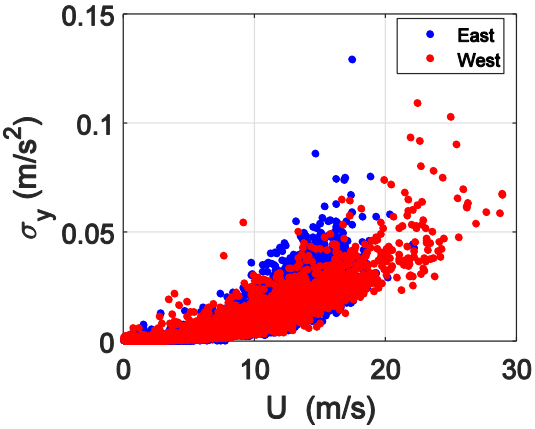

376 (b)

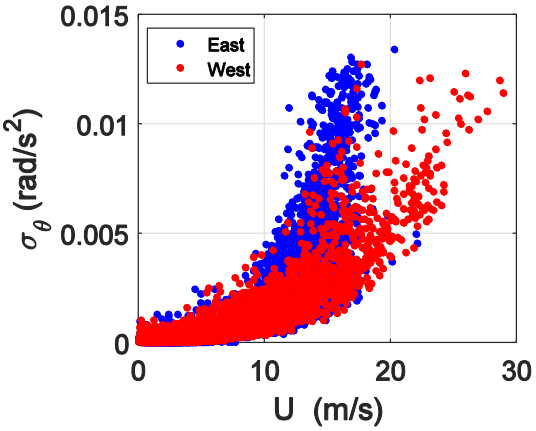

(c)

Fig. 18. RMS acceleration response vs. mean wind velocity for easterly and westerly winds: (a) RMS vertical acceleration, (b) RMS lateral acceleration and (c) RMS torsional acceleration

6. Influential factors for the dynamic response

The scatter plots given in Fig. 17 indicate severe variability in the wind-induced vibrations of the Hardanger Bridge. Since dynamic wind effects are crucially important in the design of slender cable-supported bridges, this variability should be further investigated. Identifying the sources of variability observed in the field measurements provide insight for evaluating the previously presented theoretical considerations. For this purpose, Response Surface Methodology (RSM), a well-known statistical tool [37], was utilized to study the relationship between the wind field parameters and the dynamic response. Within the framework of RSM, the physical phenomenon of wind-induced bridge response can be treated as an empirical model where the response function, its functional form and the variables involved are unknown. Because wind effects are the primary focus in this study, several parameters related to the wind field characteristics (most of which are introduced in Section 2) were selected as the variables potentially influencing the dynamic response and were included in the analysis. These are listed as:

- the mean wind speed (U, averaged over 10 mins)
- the wind yaw angle (α_{yaw})
- the standard deviations of the turbulence components (σ_u, σ_v, σ_w)
- the covariance of the u and w components of turbulence (σ_{uw})

- the along-wind and the vertical turbulence length scales (L_u, L_w)
- the vertical angle of attack (β)
- the standard deviation of the mean wind speed values measured at eight locations along the bridge (σ_{ms})
- Decay coefficients of coherence of turbulence components (C_u, C_w)

The decay coefficients are calculated by fitting Davenport's [38] coherence formula to the field data in least-squares sense. The coherence formula can be written as:

$$Coh_{u,w}(f,\Delta x) = \exp(-C_{u,w}\frac{f.\Delta x}{U}) \quad (6)$$

where f is frequency, $C_{u,w}$ are the decay coefficients and Δx is the spanwise separation. The length scale parameters (L_u, L_w) used in the analyses were calculated using method 2 described in section 4.4, due to its more common use in the practice. The final variable in the list was included to provide a crude representation of the inhomogeneity of the wind field. These variables are referred to as the predictor variables, adapting the terminology of RSM. Several sources of variability that were observed in the response measurement were not included in the analysis: the traffic loading, the spatial distribution of the wind turbulence effects, non-stationarity of the wind time series and cable vibrations. When standard stationarity tests such as the run test [39,40] are conducted on the entire data, it is found that very few recordings can be classified as stationary. Non-stationary winds can cause higher or lower bridge response compared to stationary winds with similar statistics, depending on the nature of the non-stationarity. This naturally imposes additional variability when assessing the wind and response relationship. However, analytical studies on non-stationary buffeting response of different bridge structures [41,42] show that the variations induced by non-stationary wind records are much smaller than the variability observed in the response of the Hardanger Bridge, which is mainly due to terrain effects. The wind rose plots of Fig. 16 show that the response was highly dependent on the mean wind direction, which was presumably a topographic influence on the wind field. Because this relationship between the mean wind direction and the response parameters could not be modeled using a quadratic response surface, the angle between the mean wind and the perpendicular bridge directions (yaw angle, α_{yaw}) was used in the analysis to represent the directional effects. Although the effects of topography

could not be fully represented by the yaw angle, they were partly represented by other parameters, such as the standard deviations of the turbulence and length scales, which are already dependent on the wind direction. The anemometer A6 and the accelerometer pair H5 were selected to study the wind field – bridge response relationship using response surface analysis, which are both located approximately at the midspan. However, when the analysis is repeated with another accelerometer pair, say at the quarter-span (H3 pair) considering that the first vertical mode is antisymmetric, very similar results were obtained.

A quadratic response surface including interaction terms was then fitted to the field data. The functional form of the model can be written as

$$y = \beta_0 + \sum_{i=1}^{n}\left(\beta_i x_i + \sum_{j=i+1}^{n} \beta_{ij} x_i x_j + \beta_{ii} x_i^{\,2} \right) \tag{7}$$

where n is the number of predictor variables and β represents the coefficients to be determined by a least-squares fit to the measured response. The regression is still linear because the model is linear in the coefficients [33]. The unnecessary terms should be eliminated to obtain more significant and computationally efficient response surfaces. For this purpose, after an initial fit, the predictor variables, which had negligible effect on the regression, were determined through hypothesis tests on the regression coefficients. The null hypothesis of H_0: $\beta = 0$ (the term has no effect on the model) was tested for each parameter used in the model by a t-test, and the corresponding term was deleted from the model if the null hypothesis was not rejected at a 95% significance level.

The resulting response surfaces were then used to calculate the predicted response using the field data. A summary of the regression analyses results is given in Table 2. The results of the response surface prediction are given in Fig. 19 and are plotted against the mean wind velocity. The plots indicate that most of the variability observed in the measurement data (Fig. 17) can be explained by the variability in the wind field itself. The R^2 values of the regression were 0.95, 0.9 and 0.82 for the vertical, lateral and torsional acceleration responses, respectively, which supports the previous statement. Furthermore, the significance of the regression was assessed using an F-test with the null hypothesis of H_0: $\beta_1 = \beta_2 = \ldots = \beta_n = 0$. The null hypothesis states that there is no linear relationship between the response variable and any subset of the predictor variables. The F-statistics resulting from the tests on the vertical, lateral

and torsional response surface fits were well above the test value corresponding to the 99% significance level, implying that the regressions were very significant.

It is also beneficial to elaborate on the factors that influence the response as well as their influence and interactions. Therefore, the significance of each term used in the final models was assessed, using an analysis of variance (ANOVA) procedure. The p-value approach is used to present the results instead of directly using the F-statistic due to its ease of interpretation. If the resulting p-value is less than the significance level (α), then the null hypothesis will be rejected, meaning that the term is significant at that level. The p-values calculated for the terms in the three response surfaces are given in Table 3.

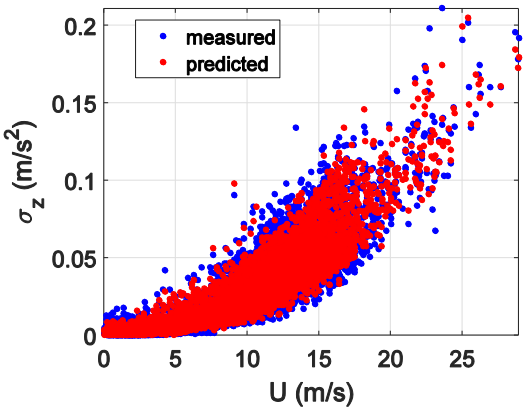

(a)

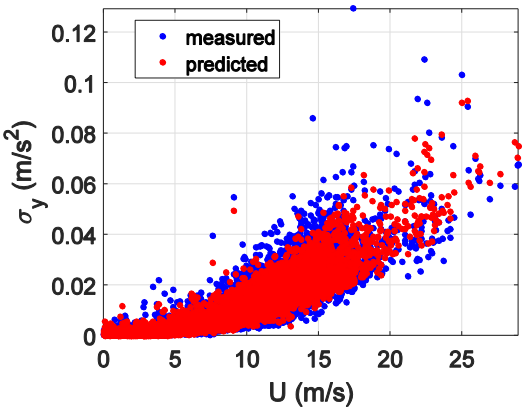

(b)

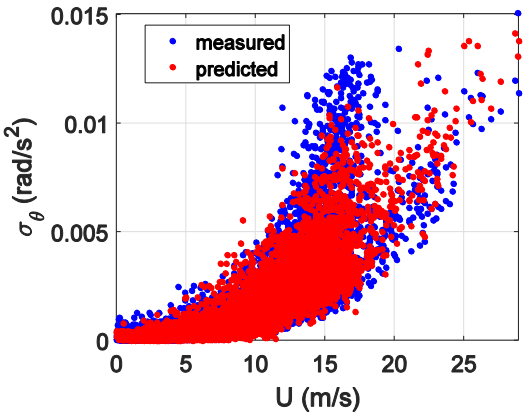

(c)

Fig. 19. Measured vs. predicted responses using the response surface models: (a) vertical response, (b) lateral response and (c) torsional response

Table 2
Summary of regression analyses

	Number of observations	R^2 value	F-statisitc for model significance
Vertical acceleration	9590	0.95	7.38 x 10^3
Lateral acceleration	9590	0.9	2.89 x 10^3
Torsional acceleration	9590	0.82	1.55 x 10^3

Table 3
Significance of terms in response surface analyses

Vertical acceleration		Lateral acceleration		Torsional acceleration	
Term	p-value	Term	p-value	Term	p-value
$U.\sigma_w$	0	$U.\sigma_w$	7.24E-206	$U.\sigma_v$	2.35E-164
U^2	2.26E-155	$\alpha_{yaw}.\sigma_u$	6.97E-65	U^2	4.25E-82
$\sigma_w.\alpha_{yaw}$	8.59E-73	$\sigma_w.L_u$	2.89E-33	U	1.18E-79
$U.C_w$	1.46E-56	$U.C_u$	8.65E-33	$L_u.\sigma_v$	8.92E-70
σ_{uw}^2	7.42E-40	U^2	7.50E-25	σ_{uw}^2	5.58E-63
U	1.97E-35	$\sigma_w.\sigma_{ms}$	7.87E-24	$U.C_w$	7.02E-58
$\sigma_w.\sigma_{ms}$	4.62E-23	σ_{uw}^2	4.35E-22	$U.\sigma_w$	1.92E-52
$\sigma_w.\sigma_v$	6.92E-23	$\sigma_w.\sigma_u$	1.66E-21	$U.\alpha_{yaw}$	1.02E-49

$\alpha_{yaw}.L_w$	1.13E-16	$\sigma_w.L_w$	2.01E-18	$\sigma_u.\sigma_{uw}$	2.13E-37
L_w^2	3.61E-16	$U.\beta$	1.30E-17	$L_w.\sigma_v$	1.18E-27
$\sigma_w.L_u$	3.87E-16	$\alpha_{yaw}.\sigma_v$	2.28E-17	$U.L_w$	8.04E-22
$\sigma_w.L_w$	6.09E-14	$\sigma_u.\sigma_{uw}$	4.15E-12	C_u	1.95E-13
$\sigma_v.\sigma_{ms}$	6.97E-13	C_w	1.28E-10	C_u^2	1.67E-12
C_w^2	5.59E-12	L_w^2	4.64E-10	$L_u.L_w$	6.77E-12
$\sigma_u.\sigma_{uw}$	9.86E-11	$\alpha_{yaw}.L_w$	5.07E-10	α_{yaw}^2	2.44E-10
L_w	3.27E-09	C_w^2	7.91E-10	$\alpha_{yaw}.L_u$	1.64E-09
$U.L_w$	1.18E-05	C_u^2	1.82E-08	α_{yaw}	3.40E-09
σ_{uw}	3.38E-05	L_w	2.06E-08	σ_w^2	6.41E-09
		$\sigma_u.\beta$	1.56E-07	L_w^2	2.11E-08
		$\alpha_{yaw}.L_u$	1.76E-07	C_w^2	2.70E-06
		$\sigma_{uw}.C_w$	7.37E-07	$\sigma_w.\sigma_u$	3.34E-06
		U	1.07E-06	$L_u.C_w$	1.01E-05
		σ_{uw}	9.97E-06		

6.1 Mean wind velocity

The tests on parameter significance showed that the mean wind velocity was the most influential factor on the dynamic response, as expected. The response surface analyses indicate a quadratic relationship between the mean wind velocity and the response, as shown in the scatter plots of Fig. 17. However, considering the R^2 values, the mean speed alone can only explain 84%, 78% and 63% of the variability in the vertical, lateral and torsional acceleration response, respectively. Accordingly, including other variables in the analyses is necessary for better describing the dynamic response.

6.2 Turbulence

The effect of the turbulence components on the dynamic response was incorporated into the response surface analyses using the standard deviations of the three turbulence components (σ_u, σ_v, σ_w) along with the covariance of the along-wind and vertical turbulences (σ_{uw}). A quick inspection of the p-values

shows that the vertical turbulence component had an important influence on all response components. The cross-wind turbulence appeared to be important only for the torsional response, whereas the along-wind turbulence was significant for both the lateral and vertical responses. The covariance term (σ_{uw}) was significant for the vertical and torsional responses but not for the lateral response.

After establishing the important terms, the effect of the four turbulence terms on the dynamic response can be investigated further. The dynamic response was predicted using the previously obtained response surfaces for a range of turbulence values. The results shown in Fig. 20 were obtained by changing only one variable while the other parameters in the model were taken as their mean values, except for the mean wind velocity, which was taken as 15 m/s and the wind yaw angle, which was taken as zero (perpendicular to the bridge). The confidence intervals (95%) for the predictions are also shown using dashed lines. The acceleration results were normalized with the maximum observed response during the field measurements. Although the actual behavior of the multivariate response surface model is more complex due to the interaction of several variables, certain inferences are possible using Fig. 20. The vertical turbulence clearly had the most profound impact on the response, while the cross-wind turbulence was equally important for the torsional response. Other turbulence components also showed a linear relationship with the response; however, their effects were much smaller in comparison. The covariance term also had a slight influence on the response. For the sake of discussion, the spectral densities of lateral, vertical and torsional forcing actions on the Hardanger Bridge section can be written using the buffeting theory [5,6] after inserting the bridge dimensions and the force coefficient terms previously obtained from wind tunnel tests [34,35] as

$$\begin{aligned} S_{yy} &= (\rho UB)^2 \left[0.014S_{uu} + 0.03S_{uw} + 0.016S_{ww}\right] \\ S_{zz} &= (\rho UB)^2 \left[0.064S_{uu} - 0.61S_{uw} + 1.62S_{ww}\right] \\ S_{\theta\theta} &= (\rho UB^2)^2 \left[0.0001S_{uu} + 0.077S_{uw} + 0.143S_{ww}\right] \end{aligned} \tag{8}$$

In the equation, ρ denotes the air density, S_{uu} and S_{ww} denote the auto-spectral densities of the along-wind and vertical turbulences and S_{uw} denotes the cross-spectral density of the u and w components and B is the width of the girder (18.3 meters). The expressions for the buffeting actions suggest that the cross-wind turbulence does not contribute to loading; this conclusion was supported by the response surface predictions except for the torsional response. The cross-spectrum S_{uw} is said to be much smaller

in comparison and is usually neglected, which was also in agreement with the findings. Moreover, the expressions show that the vertical turbulence is the most influential parameter, which was also observed in the findings. The effect of the along-wind turbulence on the lateral response was small in the response surface predictions, whereas the expressions indicated that it would be more significant. It should also be noted that in addition to the one-point statistics, the spanwise correlation of the wind loads will also effect the dynamic response, which is included in the analysis with parameters C_u and C_w. Moreover, due to the considerably long span of the bridge and the surrounding complex topography, wind loads may vary along the span, due to nonhomogeneous wind conditions. This effect was attempted to be investigated using the parameter σ_{ms}.

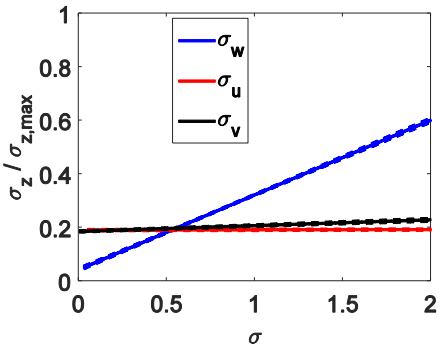

(a)

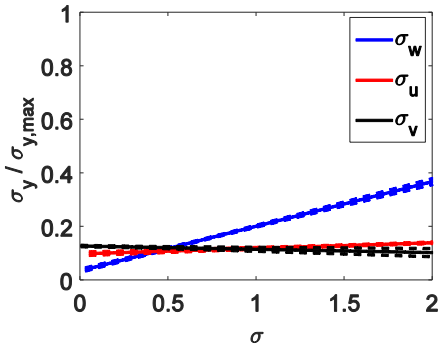

(b)

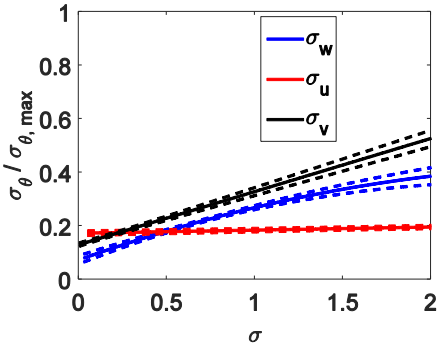

(c)

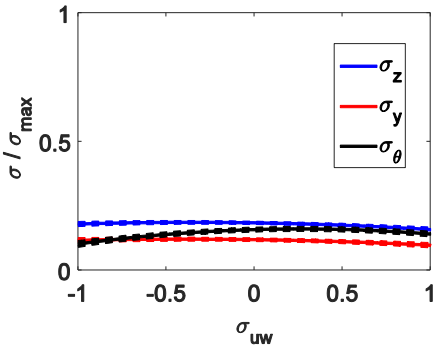

519 (d)

520 Fig. 20. Effects of turbulence on the dynamic response (the dashed lines represent 95% confidence
521 intervals): (a) vertical response, (b) lateral response, (c) torsional response and (d) covariance of u and
522 w components

523 In many cases, the turbulence terms seem to interact with each other and with other terms in the response
524 surfaces (Table 3). Some of the important interactions are presented in Fig. 21 using three-dimensional
525 surfaces. This time, the values of two variables were altered while all others remained fixed to obtain
526 the results. The surfaces given in the plots were obtained by using the fitted response surfaces for a
527 range of mean speed and turbulence values. The correlation between wind and response parameters
528 were aimed to be presented using quadratic surfaces, therefore any marginal relationship or local effects
529 may not be captured. Because the mean wind speed was the most significant variable in the model, the
530 interactions of the turbulence terms with the wind speed are of particular interest. The surface plots
531 support the relationships given in Fig. 21 for a wide range of mean speed values. All findings indicate
532 that the wind velocity fluctuations had a crucial role in the dynamic excitation of the Hardanger Bridge.

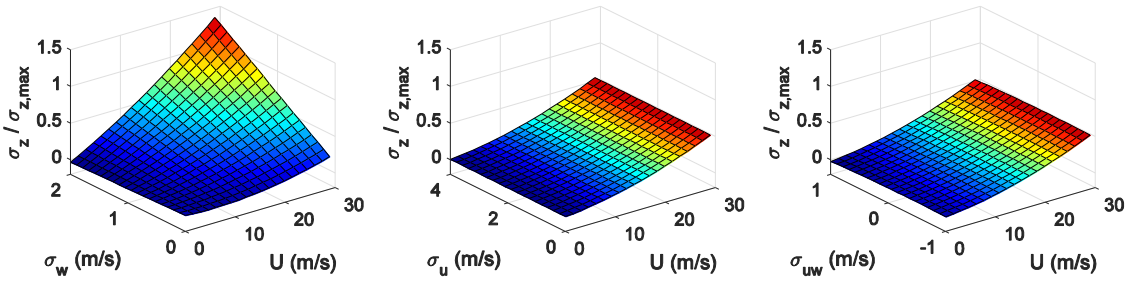

533 (a)

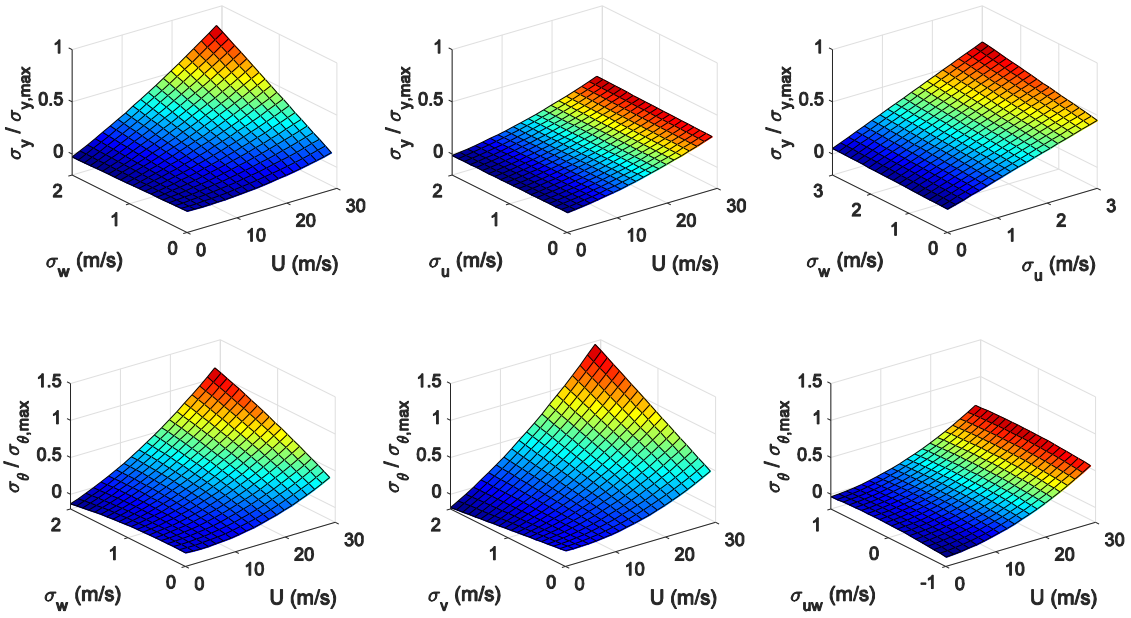

Fig. 21. Interaction effects of the turbulence components on the dynamic response: (a) vertical response, (b) lateral response and (c) torsional response

6.3 Wind yaw angle

The strong winds attacked the Hardanger Bridge was not essentially perpendicular to the bridge axis. The mean wind directions averaged over 10-minute intervals exhibited deviations from the perpendicular direction of up to 60˚ (Fig. 9). Traditionally, these skew-winds are treated as less critical events than the perpendicular winds [9,17]. This assumption relies on the decomposition of the mean wind vector to its components, which are parallel and perpendicular to the bridge axis. The effect of the parallel component to the bridge response is usually neglected where the perpendicular component is always smaller than the mean wind speed.

Instead of the traditional approach, the mean wind speed was included in the response surface analyses without any decomposition. The yaw angle (α_{yaw}) is the angle between the mean wind direction and the axis perpendicular to the bridge direction and was therefore included in the analyses. However, recent studies indicated that similar response levels can be obtained under skew-winds and perpendicular winds with the same wind speeds [9]. The response surface predictions also showed similar response levels under skew-winds and perpendicular winds.

6.4 Other Factors

The remaining factors, which have not been mentioned in the previous sections, are discussed here. The angle of attack almost completely disappeared from the response surface models after the parameter significance tests; therefore, no significant correlation could be extracted. The length scales, on the other hand, appeared in several model terms. The effect of the length scales on the response, however, was not profound, with the exception of the effect of the vertical length scale on the torsional response (Fig. 22). The models generally predicted higher responses for lower length scales, but the effect was minor. The last parameter considered in the analyses was the standard deviation of the mean wind speeds along the bridge. The effect of this parameter on the dynamic response was found to be negligible.

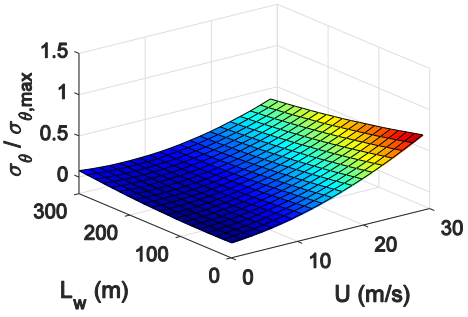

Fig. 22. Effect of the vertical length scale on the torsional response

It is also seen that the spanwise correlation of the turbulence components, represented here by the decay coefficients, had influence on the measured responses (Fig. 23). An increase in the parameters C_u and C_w (smaller spanwise correlation of turbulence) are associated with lower lateral and vertical responses, respectively. A significant correlation between the torsional response component and the C_w parameter is also observed (Fig. 23); however, with the opposite effect. When the recordings with both high C_w values and high torsional response are inspected further, it is seen that the torsional responses in such events were not dominated by the fundamental symmetric torsional mode, but had significant contributions from multiple structural modes, especially the higher modes. Nevertheless, it should be noted that correlation does not necessarily imply causation in regression analysis.

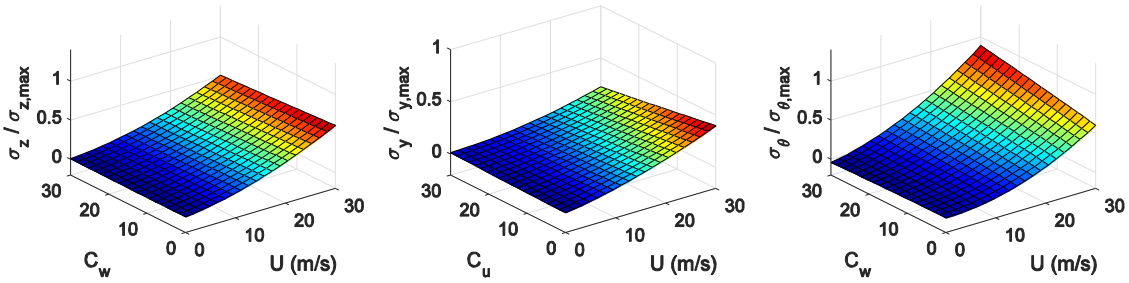

Fig. 23. Effect of decay coefficients on the dynamic response: (a) vertical response, (b) lateral response and (c) torsional response

7. Conclusions

The wind and dynamic response characteristics of the Hardanger Bridge as well as their relationship were studied using field measurement data. The following conclusions were deduced from the results:

- The wind field showed large variability in the mean wind speed, mean wind direction, turbulence intensities and length scales.
- The dynamic response of the Hardanger Bridge was governed by the low-frequency vibrations induced by the wind effects when the mean wind speed was higher than 8 m/s. In case of lower wind speeds, the vibrations induced by traffic and other sources were relatively more significant.
- The measurement data and the complementary analyses showed that high response levels were reached also under skew-wind conditions. Such wind effects should be more carefully handled in the design stage, especially when complex topographical conditions are present.
- Response surface analyses showed that most of the variability observed in response was due to variability in the wind field itself. In general, the mean wind speed and the turbulence intensities are found critical to describe the response; however, other wind-related parameters also aided in explaining the variability.
- High mean wind speed and turbulent fluctuations were associated with higher bridge response. Spanwise correlation of turbulence were also found to be correlated with the bridge dynamic response, except for the torsional response, where an inverse correlation was observed.

- Although there is significant agreement between the findings here and the prediction methods used in practice, selection of the mean wind speed as the sole design parameter fails to capture the actual variability in the wind field. Therefore, the uncertainty in the description of the wind field is suggested to be considered when designing new bridges to achieve more reliable bridge designs.
- The present investigation provides insight into prediction discrepancies using Hardanger Bridge data as an example. Further research is needed to develop methods that incorporate uncertainty in both short- and long-term response estimation methods.

8. Acknowledgments

The research described in this paper was financially supported by the Norwegian Public Roads Administration.

REFERENCES

[1] Miyata T. Historical view of long-span bridge aerodynamics. J Wind Eng Ind Aerodyn 2003;91:1393–410. doi:10.1016/j.jweia.2003.09.033.

[2] Larsen A, Esdahl S, Andersen JE, Vejrum T. Storebælt suspension bridge – vortex shedding excitation and mitigation by guide vanes. J Wind Eng Ind Aerodyn 2000;88:283–96. doi:10.1016/S0167-6105(00)00054-4.

[3] Larsen A, Larose GL. Dynamic wind effects on suspension and cable-stayed bridges. J Sound Vib 2015;334:2–28. doi:10.1016/j.jsv.2014.06.009.

[4] Brownjohn JMW, Magalhaes F, Caetano E, Cunha A. Ambient vibration re-testing and operational modal analysis of the Humber Bridge. Eng Struct 2010;32:2003–18. doi:10.1016/j.engstruct.2010.02.034.

[5] Davenport AG. Buffeting of a suspension bridge by storm winds. J Struct Div 1962;88:233–68. doi:10.4319/lo.2013.58.2.0489.

[6] Simiu E, Scanlan RH. Winds Effects on Structures: Fundamentals and Applications to Design. 3rd ed. Wiley; 1996.

621 [7] Mann J. The spatial structure of neutral atmospheric surface-layer turbulence. J Fluid Mech
622 2006;273:141. doi:10.1017/S0022112094001886.
623 [8] Tamura Y, Kareem A. Advanced Structural Wind Engineering. Springer Japan; 2013.
624 [9] Xu Y-L. Wind Effects on Cable-Supported Bridges. John Wiley & Sons; 2013.
625 [10] Kaimal JCJ, Wyngaard JCJ, Izumi Y, Coté OR, Cote OR. Spectral Characteristics of Surface-
626 Layer Turbulence. Q J … 1972;98:563–89. doi:10.1002/qj.49709841707.
627 [11] von Karman T. Progress in the statistical theory of turbulence. Proc Natl Acad Sci U S A
628 1948;34:530–9. doi:10.1073/pnas.34.11.530.
629 [12] Hui MCH, Larsen A, Xiang HF. Wind turbulence characteristics study at the Stonecutters Bridge
630 site: Part I-Mean wind and turbulence intensities. J Wind Eng Ind Aerodyn 2009;97:22–36.
631 doi:10.1016/j.jweia.2008.11.002.
632 [13] Hui MCH, Larsen A, Xiang HF. Wind turbulence characteristics study at the Stonecutters Bridge
633 site: Part II: Wind power spectra, integral length scales and coherences. J Wind Eng Ind Aerodyn
634 2009;97:48–59. doi:10.1016/j.jweia.2008.11.003.
635 [14] Brownjohn JMW, Bocciolone M, Curami A, Falco M, Zasso A. Humber bridge full-scale
636 measurement campaigns 1990-1991. J Wind Eng Ind Aerodyn 1994;52:185–218.
637 doi:10.1016/0167-6105(94)90047-7.
638 [15] Wang H, Li A, Niu J, Zong Z, Li J. Long-term monitoring of wind characteristics at Sutong
639 Bridge site. J Wind Eng Ind Aerodyn 2013;115:39–47. doi:10.1016/j.jweia.2013.01.006.
640 [16] Cao S, Tamura Y, Kikuchi N, Saito M, Nakayama I, Matsuzaki Y. Wind characteristics of a
641 strong typhoon. J Wind Eng Ind Aerodyn 2009;97:11–21. doi:10.1016/j.jweia.2008.10.002.
642 [17] Xu YL, Zhu LD. Buffeting response of long-span cable-supported bridges under skew winds.
643 Part 2: case study. J Sound Vib 2005;281:675–97. doi:10.1016/j.jsv.2004.01.025.
644 [18] Solari G, Piccardo G. Probabilistic 3-D turbulence modeling for gust buffeting of structures.
645 Probabilistic Eng Mech 2001;16:73–86. doi:10.1016/S0266-8920(00)00010-2.
646 [19] Kareem A. Aerodynamic response of structures with parametric uncertainties. Struct Saf
647 1988;5:205–25. doi:10.1016/0167-4730(88)90010-0.
648 [20] Solari G. Wind-excited response of structures with uncertain parameters. Probabilistic Eng

649 Mech 1997;12:75–87. doi:10.1016/S0266-8920(96)00027-6.
650 [21] Caracoglia L. Influence of uncertainty in selected aerodynamic and structural parameters on the
651 buffeting response of long-span bridges. J Wind Eng Ind Aerodyn 2008;96:327–44.
652 doi:10.1016/j.jweia.2007.08.001.
653 [22] Cross EJ, Koo KY, Brownjohn JMW, Worden K. Long-term monitoring and data analysis of
654 the Tamar Bridge. Mech Syst Signal Process 2013;35:16–34. doi:10.1016/j.ymssp.2012.08.026.
655 [23] Peeters B, Couvreur G, Razinkov O, Kündig C, van der Auweraer H, de Roeck G. Continuous
656 monitoring of the Øresund Bridge: System and data analysis. Struct Infrastruct Eng 2009;5:395–
657 405. doi:10.1080/15732470701478362.
658 [24] Caetano E, Cunha A, Moutinho C, Magalhães F. Dynamic characterization and continuous
659 dynamic monitoring of long span bridges. Int. Conf. Multi-Span Large Bridg., Porto, Portugal:
660 CRC Press/Balkema; 2015, p. 771–80.
661 [25] Wang H, Li A, Guo T, Xie J. Field measurement on wind characteristic and buffeting response
662 of the Runyang Suspension Bridge during typhoon Matsa 2009;52:1354–62.
663 doi:10.1007/s11431-008-0238-y.
664 [26] Wang H, Li A, Hu R. Comparison of Ambient Vibration Response of the Runyang Suspension
665 Bridge under Skew Winds with Time-Domain Numerical Predictions. J Bridg Eng 2011.
666 doi:10.1061/(ASCE)BE.1943-5592.0000168.
667 [27] Macdonald JHG. Evaluation of buffeting predictions of a cable-stayed bridge from full-scale
668 measurements. J Wind Eng Ind Aerodyn 2003;91:1465–83. doi:10.1016/j.jweia.2003.09.009.
669 [28] Wang H, Hu R, Xie J, Tong T, Li A. Comparative study on buffeting performance of sutong
670 bridge based on design and measured spectrum. J Bridg Eng 2013;18:587–600.
671 doi:10.1061/(ASCE)BE.1943-5592.0000394.
672 [29] Øiseth O, Rönnquist A, Kvåle KA, Sigbjörnsson R. Monitoring wind velocities and dynamic
673 response of the hardanger bridge. Conf. Proc. Soc. Exp. Mech. Ser., vol. 2, 2015, p. 117–25.
674 doi:10.1007/978-3-319-15248-6_13.
675 [30] Wang H, Wu T, Tao T, Li A, Kareem A. Measurements and analysis of non-stationary wind
676 characteristics at Sutong Bridge in Typhoon Damrey. J Wind Eng Ind Aerodyn 2016;151:100–

677 6. doi:10.1016/j.jweia.2016.02.001.
678 [31] Xu YL, Chen J. Characterizing nonstationary wind speed using empirical mode decomposition.
679 J Struct Eng 2004;130:912–20.
680 [32] Chen J, Hui MCH, Xu YL. A comparative study of stationary and non-stationary wind models
681 using field measurements. Boundary-Layer Meteorol 2007;122:105–21. doi:10.1007/s10546-
682 006-9085-1.
683 [33] Tennekes H, Lumley JL. A First Course in Turbulence. Cambridge: The MIT Press; 1999.
684 [34] Shuyang C, Nishi A, Hirano K, Ozono S, Miyagi H, Kikugawa H, et al. An Actively Controlled
685 Wind Tunnel And Its Application To The Reproduction Of The Atmospheric Boundary Layer.
686 Boundary-Layer Meteorol 2001;101:61–76. doi:10.1023/A:1019288828837.
687 [35] Øiseth O, Rönnquist A, Sigbjörnsson R. Effects of co-spectral densities of atmospheric
688 turbulence on the dynamic response of cable-supported bridges: A case study. J Wind Eng Ind
689 Aerodyn 2013;116:83–93. doi:10.1016/j.jweia.2013.03.001.
690 [36] Welch PD. The Use of Fast Fourier Transform for the Estimation of Power Spectra: A Method
691 Based on Time Averaging Over Short, Modified Periodograms. IEEE Trans Audio
692 Electroacoust 1967;15:70–3. doi:10.1109/TAU.1967.1161901.
693 [37] Myers RH, Montgomery DC, Anderson-Cook C. Response Surface Methodology: Process and
694 Product Optimization Using Designed Experiments . Wiley Ser Probab Stat 2009:704.
695 doi:10.2307/1270613.
696 [38] Davenport AG. The spectrum of horizontal gustiness near the ground in high winds. Q J R
697 Meteorol Soc 1961;87:194–211. doi:10.1002/qj.49708737208.
698 [39] Bendat J, Piersol A. Random Data Analysis and Measurement Procedures. Meas Sci Technol
699 2000.
700 [40] Cao S, Tamura Y, Kikuchi N, Saito M, Nakayama I, Matsuzaki Y. A case study of gust factor
701 of a strong typhoon. J Wind Eng Ind Aerodyn 2015;138:52–60.
702 doi:10.1016/j.jweia.2014.12.012.
703 [41] Chen X. Analysis of multimode coupled buffeting response of long-span bridges to
704 nonstationary winds with force parameters from stationary wind. J Struct Eng (United States)

2015;141. doi:10.1061/(ASCE)ST.1943-541X.0001078.

[42] Hu L, Xu Y-L, Huang W-F. Typhoon-induced non-stationary buffeting response of long-span bridges in complex terrain. Eng Struct 2013;57:406–15. doi:http://dx.doi.org/10.1016/j.engstruct.2013.09.044.